Moisture Recharge–Discharge Cycles: A Gross Moist Stability–Based Phase Angle Perspective

VIJIT MAITHEL[a] AND LARISSA BACK[a]

[a] *University of Wisconsin–Madison, Madison, Wisconsin*

(Manuscript received 8 November 2021, in final form 26 April 2022)

ABSTRACT: Moist static energy (MSE) budgets and gross moist stability (GMS) have been widely used as a diagnostic tool to study the evolution of moisture and convection at different time scales. However, use of GMS is limited at shorter time scales because many points in the tropics have close-to-zero large-scale vertical motion at a given time. This is particularly true in the case of convective life cycles, which have been shown to exist with noise-like ubiquity throughout the tropics at intraseasonal time scales. This study proposes a novel phase angle–based framework as a process-level diagnostic tool to study the MSE budgets during these cycles. Using the GMS phase plane, a phase angle parameter is defined, which converts the unbound GMS into a finite ranged variable. The study finds that the convective life cycles are closely linked to evolution of moisture and effectively behave as moisture recharge–discharge cycles. Convective cycles in different datasets are studied using TOGA COARE, a mix of different satellite products and ERA-Interim. Analysis of the MSE budget reveals that the cyclic behavior is a result of transitions between wet and dry equilibrium states and is similar across different regions. Further, vertical and horizontal advection of MSE are found to act as the primary drivers behind this variability. In contrast, nonlinearities in the radiative and surface flux feedbacks are found to resist the convective evolution. A linearized model consistent with moisture mode dynamics is able to replicate the recharge–discharge cycle variability in TOGA COARE data.

SIGNIFICANCE STATEMENT: In the tropics, variability of moisture and rainfall are closely linked to each other. Through this study we aim to better understand the evolution of moisture in observed daily time series data. We present a novel phase angle–based diagnostic tool to represent and study the energy budget of the system at this time resolution. Our results suggest that similar processes and mechanisms are relevant across different regions and at different scales in the tropics with moisture dynamics being important for these processes. Further, a key role is played by the energy transport associated with the large-scale circulation that drives moisture evolution in a cyclic pattern.

KEYWORDS: Tropics; Vertical motion; Oscillations; Precipitation; Advection; Cloud radiative effects; Energy budget/balance; Water vapor; Satellite observations; Reanalysis data

1. Introduction

Convective phenomena in the tropics are the result of complex interactions between convection itself, and the large-scale environment. These phenomena, observed at different spatial and temporal scales, can often be associated with at least one of the two broad type of instabilities: the moisture mode instability, which is due to the relationship between moisture and precipitation (Raymond and Fuchs 2007), and the instabilities associated with the various convectively coupled linear wave modes (Matsuno 1966; Kiladis et al. 2009). Moisture mode–based theories have found great success in explaining the slower convective modes, in particular the Madden–Julian oscillation (MJO; Raymond and Fuchs 2009; Sobel and Maloney 2013; Adames and Kim 2016; Fuchs and Raymond 2017; and others). Moisture modes have also been associated with convective life cycles (Inoue and Back 2017; Inoue et al. 2021). However, current climate models have had a hard time simulating these interactions between moisture and circulation (Stevens and Bony 2013), and the convective variability that results from it accurately, e.g., MJO (Hung et al. 2013; Kim et al. 2014; Jiang et al. 2015; Ahn et al. 2017), and convective life cycles (Wolding et al. 2020). Therefore, there is a need for good process oriented diagnostics to study the role of moisture (and hence moisture modes) and compare theory, observations, and climate models.

Budgets of column moist static energy (MSE) or moist entropy have proved remarkably useful in studying the evolution of moisture from a process level. These budgets have helped understand how interactions between radiation, surface fluxes, and advection impact organization of convection at different time and spatial scales (Bretherton et al. 2005; Back and Bretherton 2006; Maloney 2009; Kiranmayi and Maloney 2011; Andersen and Kuang 2012; Masunaga and L'Ecuyer 2014; Wing and Emanuel 2014; Juračić and Raymond 2016; Beucler and Cronin 2016; Yasunaga et al. 2019, and many others). Gross moist stability (GMS) Γ comes out as a natural parameter and a diagnostic tool from some of these analyses, and helps address the need for process-oriented diagnostics to some extent. GMS represents the efficiency of MSE export or import in the column by advection, and is defined as the ratio of energy added or removed by the circulation divided by the amount of convection (Neelin and Held 1987; Raymond et al. 2009). Despite its effectiveness, use of GMS is complicated because it is a difficult quantity to calculate. When the amount of vertical motion is close to zero, the GMS ratio is pushed toward

Corresponding author: Vijit Maithel, maithel@wisc.edu

DOI: 10.1175/JAS-D-21-0297.1

infinity making its use difficult as a diagnostic tool. Although there are methods to overcome these limitations in calculating GMS (e.g., Hannah and Maloney 2014), studying the time evolution of GMS itself, specially at shorter time resolution is still challenging. Convective cycles are one such phenomena that is particularly plagued by this issue.

Convective cycles have been observed in satellite-based datasets (Masunaga and L'Ecuyer 2014; Inoue and Back 2017), reanalysis (Inoue et al. 2021; Wolding et al. 2020, 2022), and field campaign data (Mapes et al. 2006; Inoue and Back 2015; Hannah et al. 2016) during which convection undergoes statistical cycles of increase and decrease in large-scale upward vertical motion at time scales much longer than those associated with a typical mesoscale convective system life cycle. The ubiquitous nature of these convective cycles suggests that the mechanisms responsible for its evolution are fundamental to convection in the tropics. Furthermore, current climate models have a hard time simulating this type of variability accurately (Wolding et al. 2020). Therefore, it is important to understand the role of various column processes during the different phases of the convective cycle. During a complete cycle, large-scale upward vertical motion anomalies will transition between negative and positive values leading to GMS values becoming infinite when the magnitude of upward vertical motion is small. This restricted the scope of previous studies trying to understand these cycles through a GMS-based framework (Inoue and Back 2015) by forcing them to confine their analysis to only one-half of the cycle. This paper expands on the GMS-based framework developed in Inoue and Back (2015) and tackles these issues by defining an alternative parameter to represent the role of GMS, namely, the GMS phase angle.

Previous studies (Inoue and Back 2015, 2017; Inoue et al. 2021) utilize a GMS phase plane to study these convective cycles. The GMS phase plane, defined as the divergence of dry static energy (DSE) on the x axis versus divergence of MSE on y axis (Masunaga and L'Ecuyer 2014; Inoue and Back 2015), provides a geometric visualization of convective cycles in the form of elliptical orbits with GMS being the slope of the line connecting the origin to a point on the phase plane (Fig. 1). Then, a phase angle can be defined on the phase plane corresponding to the GMS value for a point, effectively converting the unbound slope magnitude into a finite ranged angle value. Though the transition from GMS value to GMS phase angle is not a linear transition, nevertheless, the physical interpretation of the phase angle values is similar to GMS. This paper proposes GMS phase angle as a new diagnostic tool that can be used to study these cycles in detail and compare theory, observations, and models.

During a convective cycle, when convection increases in strength, Inoue and Back (2015) refer to it as the amplifying phase and when it decreases in strength, they refer to it as the decaying phase. In terms of MSE, the increase and decrease in convective strength coincides with increase and decrease in column MSE. In the free troposphere, under the weak temperature gradient approximation (WTG; Sobel and Bretherton 2000; Sobel et al. 2001) variations in temperature are very small in the tropics. As a result, variations in column MSE are primarily associated with increase or decrease of column moisture. Therefore, the convective life cycles can also be considered as moisture or column MSE recharge–discharge cycles in this regard. The context in which the term, recharge–discharge cycles is being used here could be a bit different to how it has been used in previous studies (e.g., Chikira 2014). By recharge–discharge, we refer to changes in column moisture or MSE and the processes that contribute to it in context of describing the physical state of the large-scale environment, and not it terms of recharge–discharge of convective instability associated with convective plumes. From here on we will use convective life cycles or just convective cycles and recharge–discharge (RD) cycles interchangeably.

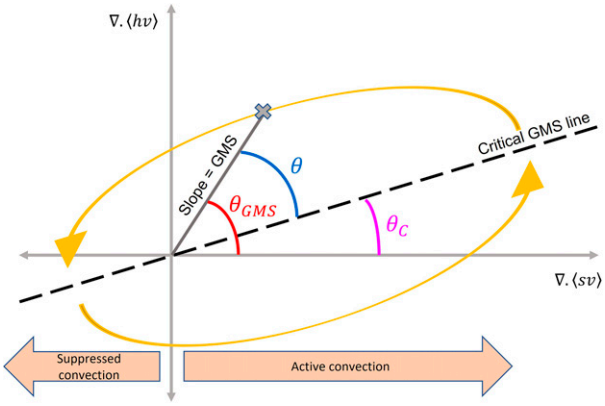

FIG. 1. Schematic showing the GMS phase plane and the various phase angles. The GMS phase angle θ_{GMS} (red) represents the MSE advection terms. Critical GMS phase angle θ_c (pink) represents the column radiation and surface flux terms. Life cycle phase angle θ (blue) is the difference between the two and represents the angle with respect to the critical GMS line. θ is related to the MSE tendency term in the MSE budget. Yellow arrows show the trajectory of a typical RD cycle on the phase plane.

We write the MSE budget equation as

$$\frac{\partial\langle Lq\rangle}{\partial t} \approx \frac{\partial\langle h\rangle}{\partial t} = -\langle\omega\partial h/\partial p\rangle - \langle \mathbf{v}\cdot\boldsymbol{\nabla}h\rangle + \langle Q_R\rangle + S, \qquad (1)$$

where h represents MSE, Lq represents moisture in energy units, Q_R represents radiative heating, S represents net surface flux, $\mathbf{v}$ represents horizontal winds, ω represents the vertical velocity, and the angle brackets $\langle\rangle$ mean mass-weighted vertical integral between the 1000 and 100 hPa pressure levels. Based on the MSE budget, changes in column moist static energy or column moisture can be associated with vertical advection ($\langle\omega\partial h/\partial p\rangle$), horizontal advection ($\langle\mathbf{v}\cdot\boldsymbol{\nabla}h\rangle$), radiative heating in the column ($\langle Q_R\rangle$), and the net surface fluxes (S), which is the sum of latent and sensible heat fluxes (LH and SH, respectively).

The diabatic terms (radiative and surface fluxes) which can be approximated as a linear feedback of convective strength (Bretherton and Sobel 2002; Su and Neelin 2002) act as a line of separation between the two phases on the GMS phase plane, which Inoue and Back (2015) called the critical GMS (black dashed line in Fig. 1). Critical GMS represents the efficiency with which diabatic terms change the column MSE.

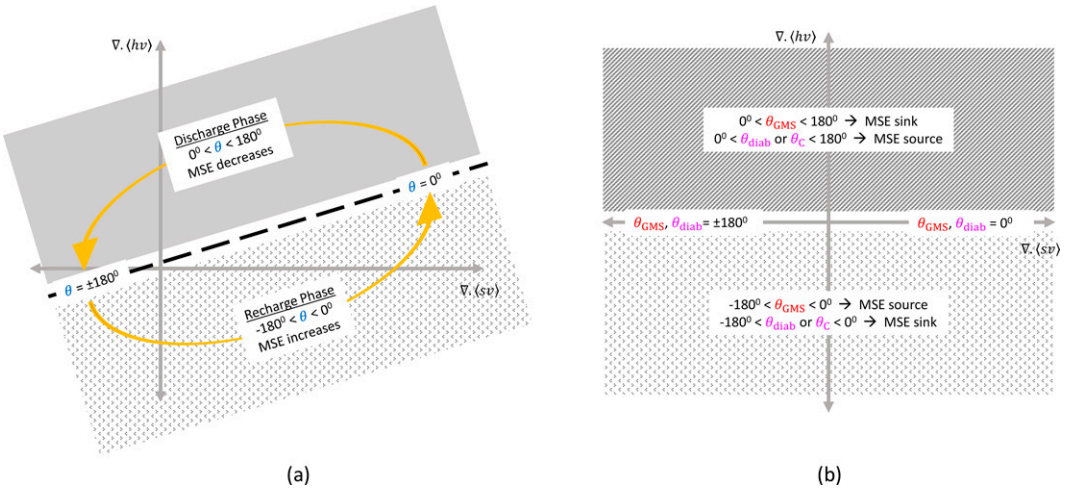

FIG. 2. Schematic showing the various phase angles on the GMS phase plane and their contribution to MSE budget. (a) Relation between life cycle phase angle θ (blue) and the recharge–discharge phases. Yellow arrows represent the direction of evolution of a typical cycle. (b) Role of critical GMS phase angle θ_c (pink) and GMS phase angle θ_{GMS} (red) as source and sink of MSE for different locations on the phase plane.

For points on the line, advection of MSE balances the diabatic terms and MSE tendency is zero. For points below this critical line, the right-hand side of Eq. (1) is positive leading to increase in moisture and convection, and for points above the line the right-hand side is negative leading to decrease in moisture tendencies (Fig. 2a) (Inoue and Back 2015, 2017). This interplay between MSE advection and the diabatic terms govern the convective variability during the life cycle and is broadly consistent with the nature of mechanisms possible for moisture evolution under WTG (Chikira 2014).

The question then arises, how does this interaction between the advective terms and the diabatic terms change during the course of the cycle and how does this impact the evolution of the RD cycle itself? Inoue and Back (2015) look at this question in the TOGA COARE dataset (Webster and Lukas 1992) by defining a drying efficiency parameter that is similar to the notion of effective GMS (e.g., Bretherton and Sobel 2002; Su and Neelin 2002; Hannah and Maloney 2014; and others). It combines the effect of advective terms on column MSE tendency with the effect of radiative feedbacks and surface fluxes. Results from Inoue and Back (2015) are restricted to only the anomalously high convective part of the cycle due to limitation of using GMS-based variables. They find that the diabatic terms have a destabilizing impact on the column that supports growth of moisture anomalies during both the amplifying and decaying phase (support convection). Horizontal and vertical advection have a varying impact importing MSE into the column during the amplifying phase (support convection) and exporting MSE out of the column during the decaying phase (inhibit convection). They also argue that vertical advection is more dominant in the amplifying phase, and horizontal advection is more dominant in the decaying phase of the life cycle. Alternatively, Inoue et al. (2021), using ERA-Interim data, show that horizontal advection is more important for predicting growth or decay of precipitation during the cycle including the amplifying phase, hypothesizing that the presence of other wave modes is responsible for the importance of vertical advection in Inoue and Back (2015). Horizontal advection is found to be more important than vertical advection in other slower modes too including damping of MJO amplitude (Wolding et al. 2016).

It should be mentioned that interpretations of the MSE budget for a cyclic or wave mode also depend on the frame of reference. Amplification or decay in a Lagrangian view corresponds to horizontal propagation of the wave in an Eulerian framework. Analysis in previous work (Inoue and Back 2015; Inoue et al. 2021; Wolding et al. 2020) and in this study follow a Lagrangian point of view that corresponds to a propagating wave mode in the Eulerian view.

A simple theoretical model for the advective terms during the convective life cycle is presented in Inoue and Back (2017) based on idealized linear moisture mode theory. The parameters of the simple model, which can be calculated based on observations, do a good job of simulating the elliptical orbits on the GMS phase plane and indicate the relevance of moisture for convective life cycle variability. Inoue et al. (2021) also highlight the similarity between the assumptions in moisture mode studies and their analysis of convective life cycles based on MSE budgets, and argue that same mechanisms as moisture modes are applicable more broadly for explaining convective variability in the tropics beyond just the MJO. Other studies have also looked at and found moisture dynamics to play an important role in explaining different aspects of tropical convective variability associated with different tropical wave modes (review by Adames and Maloney 2021).

Our present study looks in particular at the role being played by radiative fluxes, surface fluxes, vertical advection, and horizontal advection during different phases of the RD cycle using the GMS phase angle framework. Since these

cycles have been observed ubiquitously, we are particularly interested in what these results will imply about the processes related to a more general variability of convection in the tropics. We are especially interested in studying the time evolution of the cycle more explicitly than has been done in past work with the help of time derivative of phase angle. We perform the analysis for TOGA COARE data, satellite-based data, and reanalysis data to compare the RD cycles and underlying processes observed in all three datasets. Observations are also compared with an idealized model of the life cycle consistent with moisture modes to understand the contribution of moisture dynamics in governing convective variability associated with the life cycles.

Section 2 describes the datasets and data processing techniques used in this study. Section 3 presents the basic equations and the theoretical framework for the phase angle parameters and the simple model based on moisture mode theory. Section 4 presents the features and characteristics of RD cycles when analyzed using the GMS phase angle framework. Further discussions are presented in section 5, followed by concluding remarks in section 6.

2. Data and methods

This study uses observational and reanalysis datasets to study the evolution of column integrated moisture tendency and moist static energy budgets [Eq. (1)] during RD cycles. The first part of the study is carried out using a version of field campaign data from TOGA COARE (Webster and Lukas 1992), which was constrained to conserve column integrated mass, and energy quantities (Zhang and Lin 1997). This dataset, spanning the 4-month-long intensive observation period from 1 November 1992 to 28 February 1993, with a 6 h time resolution is also passed through a 24 h running-mean filter to remove the effects of diurnal cycle and ensure that the WTG approximation is valid (Inoue and Back 2015; Yano and Bonazzola 2009).

The second part of the study uses a mix of satellite-based datasets and ERA-Interim data (Dee et al. 2011) to study RD cycles over different spatiotemporal scales. We utilize a daily time series data over 8 years from 2000 to 2007 to be able to compare results directly with Inoue and Back (2017). Satellite-based datasets are used for precipitable water, radiative heating, as well as latent and sensible heat surface fluxes using the same data treatment process as Inoue and Back (2017). Precipitable water is provided by Remote Sensing Systems and is derived from the TRMM Microwave Imager (TMI; Wentz et al. 2015), Special Sensor Microwave Imager (SSMI; Wentz et al. 2012), and Advanced Microwave Scanning Radiometer for Earth Observing System (AMSR-E; Wentz et al. 2014). The radiative heating estimates are derived using the Hydrologic Cycle and Earth's Radiation Budget (HERB; L'Ecuyer and Stephens 2003, 2007) algorithm from TMI. The surface flux data were obtained from SeaFlux (Curry et al. 2004). The diurnal cycle and seasonal cycle are removed from data for all three variables and the data are regridded to a 2° × 2° horizontal resolution spatial domain. More detailed information about these data procedures can be found in section 3 of Inoue and Back (2017).

Our study differs from Inoue and Back (2017) by making use of ERA-Interim data (Dee et al. 2011) to calculate the advective terms in the moist static energy budget rather than calculating them as budget residuals. Horizontal wind fields, along with the temperature and moisture fields are used from ERA-Interim to calculate horizontal and vertical advection explicitly, which Inoue and Back (2017) did not do. The ERA-Interim data from 2000 to 2007 are also converted to a daily time series at a 2° × 2° spatial resolution, and the diurnal cycle and seasonal cycle is removed to match the satellite-based datasets. Additionally, we also pass all the data through a 10–90 day Lanczos bandpass filter with 75 weights to further remove any other short-term and long-term variability apart from the one already removed as part of the diurnal and seasonal cycle. The bandpass filter helps reduce the noise and displays the convective cycle signal better in the longer time series. Changing the number of weights does not impact the results significantly (not shown). The length of the bandpass filter is chosen arbitrarily and does not impact the results qualitatively (not shown).

For similarity, we focus our study on the four main tropical ocean basins defined in Inoue and Back (2017). These are defined by selecting grid points, with mean precipitation greater than 5 mm per day, between 5°S–5°N, 60°–90°E for Indian Ocean (IO); 5°S–5°N, 150°–180°E for western Pacific (WP); 0°–15°N, 190°–250°E for eastern Pacific (EP); and 0°–15°N, 300°–360°E for Atlantic Ocean (AO).

3. Theoretical framework

a. GMS and drying efficiency (Inoue and Back 2015)

Because advection of MSE can also change with changing amount of convection, in addition to changing gradients of MSE, it makes sense for many purposes to normalize column MSE advection per unit of convection. This introduces GMS, Γ ($=\nabla\cdot\langle h\mathbf{v}\rangle/(\nabla\cdot\langle s\mathbf{v}\rangle)$ in our analysis as the MSE budget becomes

$$\frac{\partial\langle Lq\rangle/\partial t}{\nabla\cdot\langle s\mathbf{v}\rangle}=-\frac{\nabla\cdot\langle h\mathbf{v}\rangle}{\nabla\cdot\langle s\mathbf{v}\rangle}+\frac{\langle Q_R\rangle+S}{\nabla\cdot\langle s\mathbf{v}\rangle}. \tag{2}$$

Here, s represents DSE, $\nabla\cdot\langle s\mathbf{v}\rangle$ represents total advection of DSE, and $\nabla\cdot\langle h\mathbf{v}\rangle$ is the total advection of MSE given by the sum of vertical and horizontal advection of MSE. DSE advection, $\nabla\cdot\langle s\mathbf{v}\rangle$ can be used as a metric for amount of convection in the normalization above. The dominant balance in the DSE budget [Eq. (3)] is between the advective term and convective heating, LP (P is amount of precipitation):

$$\nabla\cdot\langle s\mathbf{v}\rangle=\langle Q_R\rangle+LP+\mathrm{SH}. \tag{3}$$

Since the column radiative heating and surface fluxes are proportional to P, the terms on the right-hand side in Eq. (3) can be combined together and $\nabla\cdot\langle s\mathbf{v}\rangle$ can be linked to amount of precipitation. Inoue and Back (2015) define the right-hand side of Eq. (2) in terms of the drying efficiency

parameter, $\Gamma - \Gamma_C$ where Γ_C is the critical GMS defined as $\Gamma_c = (\langle Q_R \rangle + S)/(\nabla \cdot \langle s\mathbf{v} \rangle)$. While Γ represents the impact of advective terms in the MSE budget, Γ_C represents the impact of the diabatic fluxes (column radiation and surface flux):

$$\frac{\partial \langle Lq \rangle / \partial t}{\nabla \cdot \langle s\mathbf{v} \rangle} = -(\Gamma - \Gamma_c). \tag{4}$$

During the convectively active phase ($\nabla \cdot \langle s\mathbf{v} \rangle > 0$) of the cycle, when drying efficiency is negative moisture anomalies increase, and when drying efficiency is positive moisture anomalies decrease. This makes drying efficiency a useful diagnostic tool. However, as highlighted earlier, the usefulness of drying efficiency is restricted because the value is not well defined when amount of upward vertical motion (as defined by dry static energy advection) is small, as is often the case in tropics which are close to radiative–convective equilibrium.

b. *Transitioning to phase angles*

This issue is tackled by defining phase angle parameters on the GMS phase plane. As mentioned previously, GMS and GMS-like quantities, which represent the slope of a line on the GMS phase plane, can be easily transformed into an angle value (Fig. 1). This is done by computing the arc tangent of the relevant GMS-like quantity. The resulting angle value can be easily interpreted physically in terms of GMS using the phase plane, and at the same time it is well defined throughout the time series and can be used for other analysis.

Since the critical GMS line acts as the boundary between the recharge and the discharge phase, the life cycle phase angle, θ is defined as the angle between the line connecting a point to the origin and the critical GMS line (blue angle in Fig. 1). The life cycle phase angle θ value then represents whether a point lies below the critical GMS line or above it, and is analogous to drying efficiency in Inoue and Back (2015). Geometrically from Fig. 1,

$$\theta = \theta_{\mathrm{GMS}} - \theta_c, \tag{5}$$

where

$$\theta_{\mathrm{GMS}} = \arctan\left(\frac{\nabla \cdot \langle h\mathbf{v} \rangle}{\nabla \cdot \langle s\mathbf{v} \rangle}\right) \quad \text{and} \tag{6}$$

$$\theta_c = \arctan\left(\frac{\widehat{\langle Q_R \rangle + S}}{\nabla \cdot \langle s\mathbf{v} \rangle}\right). \tag{7}$$

Here, θ_{GMS} is called the GMS phase angle, and θ_c is called the critical GMS phase angle, and $\widehat{\langle Q_R \rangle + S}$ represent linearly regressed diabatic fluxes ($\langle Q_R \rangle + S$) on ($\nabla \cdot \langle s\mathbf{v} \rangle$). The GMS phase angle represents the efficiency of the advective term in transporting MSE and the critical GMS phase angle represents the efficiency of radiative heating and surface fluxes terms.

Equation (5) makes use of the observation that the diabatic fluxes can be well approximated through a linear regression line (Inoue and Back 2017) to calculate the life cycle phase angle. An alternate method can be to calculate a single arc tangent value of the full right-hand side of Eq. (2). Life cycle phase angle values calculated through both the methods are closely correlated with one another (not shown). Using Eq. (5) has the advantage that impact of advective and diabatic terms can be calculated explicitly.

The critical GMS phase angle, θ_c calculated as per Eq. (7) is a constant for a given diabatic flux time series and does not impact how the life cycle phase angle will evolve with time. However, the underlying diabatic flux terms can vary in time. These can be represented by defining a time varying diabatic flux phase angle θ_{diab} using the following equation:

$$\theta_{\mathrm{diab}} = \arctan\left(\frac{\langle Q_R \rangle + S}{\nabla \cdot \langle s\mathbf{v} \rangle}\right). \tag{8}$$

Additionally, using Eq. (9), the GMS phase angle can be further broken down into vertical GMS angle θ_V and horizontal GMS angle θ_H to represent the contribution of vertical and horizontal advection, respectively:

$$\theta_V = \arctan\left(\frac{\langle \omega \partial h/\partial p \rangle}{\nabla \cdot \langle s\mathbf{v} \rangle}\right) \quad \text{and} \quad \theta_H = \arctan\left(\frac{\langle \mathbf{v} \cdot \nabla h \rangle}{\nabla \cdot \langle s\mathbf{v} \rangle}\right). \tag{9}$$

Because angles do not add up like scalars, the vertical and horizontal angles will not add up to give the GMS phase angle, unlike vertical and horizontal GMS, which add up to give total GMS. However, defining the vertical and horizontal GMS angles will allow us to study each of these terms individually in the phase angle framework.

It should be noted that the initial arc tangent values, which will range from −90° to 90°, cannot differentiate between the right (convectively active) and the left half (convectively inactive) of the phase plane. To do so the arc tangents values are modified such that the final phase angle values range from −180° to 180°. Then the phase angles cover the entire phase plane uniquely. Schematics in Fig. 2 show the range of the various phase angles and the corresponding area on the plane spanned the respective angle values.

c. *Physical interpretation of phase angle parameters*

Physically, phase angles can be interpreted just like GMS, in terms of energy transport. For example, a negative θ_{GMS} implies that the system lies below the x axis (Fig. 2b). As a result, divergence of MSE (y axis) is negative in that state and the system is importing MSE through advection. Similarly, a negative θ value will represent that the system is below the critical GMS line and hence is in the recharging phase. Figure 2 represents the relation between various phase angle values and their contribution to MSE budget. Furthermore, the magnitude of phase angle values can be used to diagnose the efficiency of the system. Higher phase angle magnitudes imply high values of MSE advection (y-axis magnitude) for small convective strength (x-axis magnitude). Therefore, these are states during which convection is highly efficient at importing or exporting MSE (large GMS magnitude). The vertical and horizontal GMS phase angles can further be understood physically in terms of vertical motion profile shape variability and horizontal

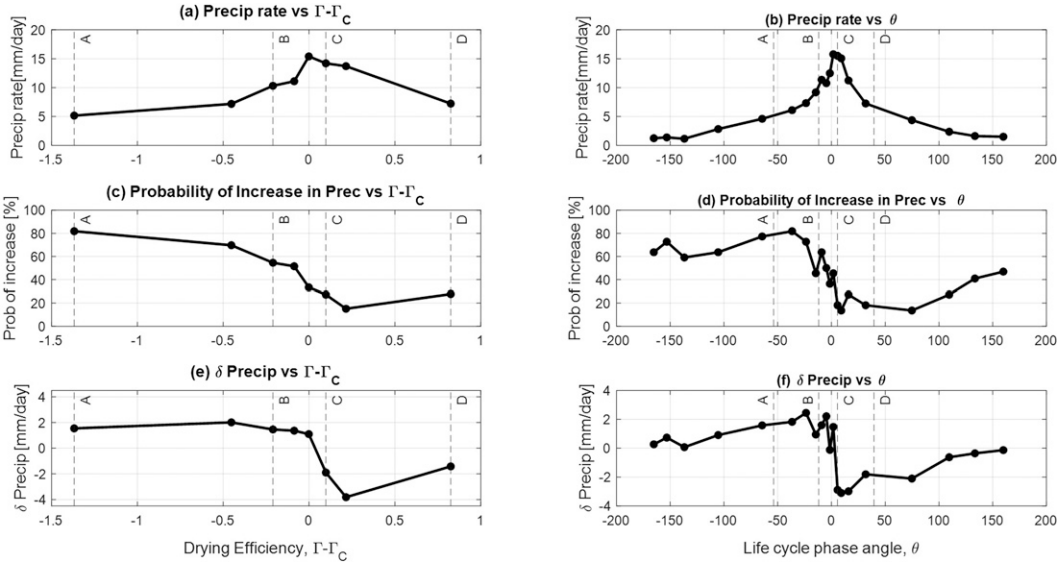

FIG. 3. (top) Precipitation rate (mm day^{-1}), (middle) probability of increase in precipitation rate with time, and (bottom) change in precipitation rate (mm day^{-1}) in TOGA COARE data as a function of binned values of drying efficiency, (left) $\Gamma - \Gamma_C$ (reproduced from Inoue and Back 2015) and (right) life cycle phase angle θ. The uppercase letters A, B, C, and D are corresponding locations of the same physical state in the different frameworks. Average error bar length for each subplot is as follows: (a) 4.2 mm day^{-1}, (b) 3.7 mm day^{-1}, (c) 36%, (d) 48%, (e) 3.6 mm day^{-1}, (f) 3.5 mm day^{-1}.

transport of moisture across gradients, respectively. These are discussed in more detail in section 5.

The relation between amplifying and decaying convective phases with the life cycle phase angle values can be further visualized in a manner similar to Fig. 4 in Inoue and Back (2015) for drying efficiency values. Precipitation rate and metrics of changes in precipitation rate are plotted against both drying efficiency and life cycle phase angle in TOGA COARE data to show that drying efficiency can easily be substituted with life cycle phase angle as the parameter used to study convective life cycles. Binned values of life cycle phase angle are plotted on the x axis and are arranged in an increasing order from $-180°$ to 180° to represent a composite life cycle. Bins are created for every 8.33rd percentile range containing 39 samples in each bin for TOGA COARE data. Following Fig. 4 from Inoue and Back (2015), Fig. 3 shows bin averaged absolute precipitation rate (top row), change in precipitation rate (bottom row), and probability of increase in precipitation rate (middle row) as functions of binned drying efficiency (left) and life cycle phase angle (right). The four vertical lines represent the corresponding location of the same state in the other parameter framework. Owing to the small number of samples in each bin, the error bars corresponding to the 95% confidence interval about the bin mean are relatively large and have been omitted to make the figure clearer. Instead, the average length of the error bars is mentioned in the figure captions. We determine the number of independent samples in the time series data by determining the e-folding time scale from the time lag autocorrelation function. Inoue and Back (2017) show that similar characteristics are also seen in a larger independent dataset, which will not have the same issue of under sampling.

As one transitions from amplifying to decaying convective phase, we expect that the absolute precipitation rates should peak at this transition as it is the end of the amplifying phase. Moreover, there should be a sharp drop-off in the probability of increase of precipitation rate as the cycle goes from amplifying to decaying phase of convection. In terms of changes in precipitation rate, δP will change from positive in amplifying phase to negative during decaying phase. This is observed as drying efficiency values change from negative to positive in Fig. 3, as also shown in Inoue and Back (2015). Similar trends are seen as life cycle phase angle value changes from negative to positive, showing the strong relation between phase angle values and the two phases of the cycle. This also points toward the advantage of using phase angle instead of drying efficiency. In case of drying efficiency, the analysis is forced to be restricted between -1.5 and 1. This corresponds to a small range in terms of phase angle value as shown by the vertical lines. Therefore, with the use of phase angles, the analysis can be easily carried out and plotted for the entire cycle.

Figure 4 represents the evolution of the vertical profiles of (Fig. 4a) anomalous moisture (top) and (Fig. 4b) anomalous moisture tendencies (bottom) as a function of the composite life cycle. The line plot shows the value of the vertically integrated moisture anomaly for the total column. The anomalous moisture tendencies are positive throughout most of the troposphere during the increasing convective phase (negative x axis). This results in the total column being anomalously moist toward the end of the amplifying phase. In contrast, the decaying convective phase (positive x axis) is dominated by negative moisture

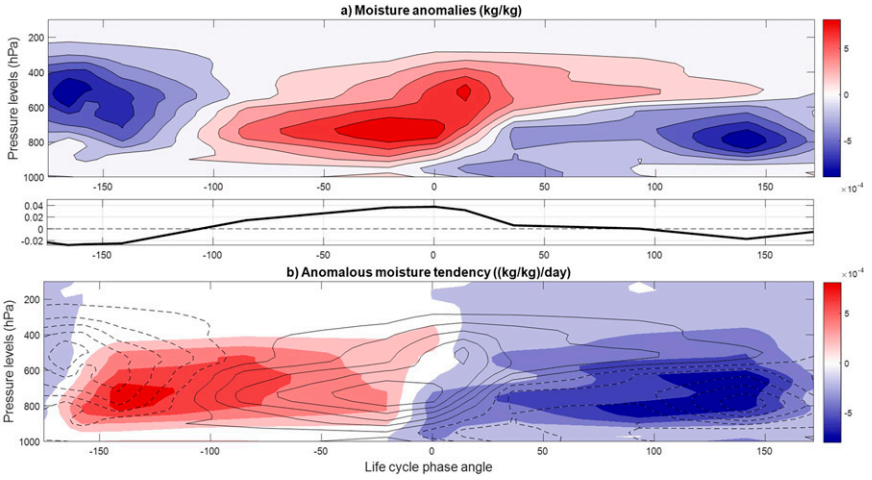

FIG. 4. (top) Anomalous moisture profiles (kg kg^{-1}) and (bottom) anomalous moisture tendencies (kg kg^{-1} day^{-1}) as a function of binned life cycle phase angle values. In the bottom panel, solid and dashed contours represent positive and negative moisture anomalies from the top panel, respectively, and color shading represents the moisture tendencies. (middle) Line plot shows the mass-weighted vertical integral of moisture anomaly profiles in (a). Negative values on x axis correspond to the recharge phase and positive values represent the discharge phase.

tendencies throughout the troposphere and result in an anomalously dry column at the end of the decreasing phase. The exact vertical structure of moisture anomalies is more detailed and consistent with previous studies (Inoue and Back 2015; Wolding et al. 2022). However, in terms of evolution of column moisture, the convective life cycle is behaving like a moisture recharge–discharge cycle, as expected from Eq. (1). Figures 3 and 4 together also imply that precipitation and column moisture are closely related to each other. This condition, along with WTG balance, forms the essence of the moisture mode criteria presented in Mayta et al. (2022). This further supports the idea that moisture dynamics are important for this convective mode.

d. Idealized model of convective cycle

Inoue and Back (2017) discuss the interpretation of the time-dependent and the time-independent GMS associated with life cycles using an idealized model to represent the vertical advection term. They show that vertical advection displays elliptical orbits on the GMS phase plane when its variability is modeled from simplified moisture mode solutions that have an imaginary component in the vertical GMS. They also show that the time-independent or the background GMS is the fixed value associated with the slope of the major axis of the ellipse and the time-dependent GMS varies as the system evolves during the cycle moving along the elliptical orbits. They also highlight that since only the background GMS is related to stability of the moisture mode, the moisture mode is stable for positive values of time-independent GMS and vice versa. Moreover, it is also possible to have negative time-dependent GMS values even in a stable moisture mode. Similar interpretation of negative GMS values is discussed in Raymond et al. (2009) for nonsteady-state conditions like the ones under which RD cycles would also be classified.

As discussed earlier, column moisture anomalies are important for the evolution of precipitation in moisture mode theories. Further, the tight coupling between column moisture anomalies and precipitation anomalies (e.g., Bretherton et al. 2004) implies that precipitation changes can be modeled in terms of precipitation anomalies in the moisture mode framework. Following Inoue and Back (2017), an idealized model can be expressed as

$$\frac{\partial P'}{\partial t} = -(\Gamma_{\mathrm{eff},r} + i\Gamma_{\mathrm{eff},i}) \times P', \tag{10}$$

where P' is precipitation anomaly, and $\Gamma_{\mathrm{eff},r}$ and $\Gamma_{\mathrm{eff},i}$ are the real and imaginary model parameters associated with growth or stability of the system and mode propagation, respectively. The model permits solutions of the form

$$P'(x,t) = \hat{P}\exp[ikx + (\sigma_r + i\sigma_i)t], \tag{11}$$

where $\hat{P}$ is an amplitude, k is a zonal wavenumber, σ_r and σ_i represent real and imaginary frequencies, respectively. We can assume $\Gamma_{\mathrm{eff},r} = 0$ since the precipitation has to be nonzero and finite over a long time series. Based on this setup, equations for the vertical and horizontal advection terms can be derived (not shown) that express how vertical and horizontal advection will evolve for a solution of the form of Eq. (11) and are given below (Inoue and Back 2017):

$$\left\langle \frac{\omega \partial h}{\partial p} \right\rangle_M \simeq \hat{P}(\Gamma_{v,r}\cos\Gamma_{\mathrm{eff},i}t + \Gamma_{v,i}\sin\Gamma_{\mathrm{eff},i}t), \tag{12}$$

$$\langle \mathbf{v}\cdot\nabla h\rangle_M \simeq \hat{P}(\Gamma_{h,r}\cos\Gamma_{\mathrm{eff},i}t + \Gamma_{h,i}\sin\Gamma_{\mathrm{eff},i}t). \tag{13}$$

Subscript M represent vertical and horizontal advection as calculated from the simple model; $\Gamma_{v,r}$ and $\Gamma_{h,r}$ are the real

part of model parameters, and are related to the background (time-independent) vertical and horizontal GMS, whereas $\Gamma_{v,i}$, $\Gamma_{h,i}$, and are the imaginary parts of model parameters associated with the time-dependent GMS. Further, these parameters can be estimated from observed data as per the following equations:

$$\Gamma_{v,r} \simeq \frac{\overline{\left\langle \frac{\omega \partial h}{\partial p} \right\rangle \times \nabla \cdot \langle s\mathbf{v} \rangle}}{\overline{\nabla \cdot \langle s\mathbf{v} \rangle}^2}, \quad \Gamma_{h,r} \simeq \frac{\overline{\langle \mathbf{v} \cdot \nabla h \rangle \times \nabla \cdot \langle s\mathbf{v} \rangle}}{\overline{\nabla \cdot \langle s\mathbf{v} \rangle}^2}, \tag{14}$$

$$\Gamma_{v,i} \simeq -\Gamma_{\mathrm{eff},i} \frac{\overline{\left\langle \frac{\omega \partial h}{\partial p} \right\rangle \times \frac{\partial \nabla \cdot \langle s\mathbf{v} \rangle}{\partial t}}}{\left(\overline{\frac{\partial \nabla \cdot \langle s\mathbf{v} \rangle}{\partial t}}\right)^2}, \quad \Gamma_{h,i} \simeq -\Gamma_{\mathrm{eff},i} \frac{\overline{\langle \mathbf{v} \cdot \nabla h \rangle \times \frac{\partial \nabla \cdot \langle s\mathbf{v} \rangle}{\partial t}}}{\left(\overline{\frac{\partial \nabla \cdot \langle s\mathbf{v} \rangle}{\partial t}}\right)^2}. \tag{15}$$

Here, the overbar denotes a time average, and $\Gamma_{\mathrm{eff},i}$ represents the frequency of the life cycle equal to $2\pi/n$, where n is the number of days it takes to complete a full cycle. The approximate value of n is calculated from data based on values of $\partial\theta/\partial t$ as outlined in the next section. The model parameters in Eqs. (14) and (15) are calculated using the complete TOGA COARE time series, and their value is used in Eqs. (12) and (13) to generate a sample time series for the advective terms as per the simple model. Readers are referred to section 5b in Inoue and Back (2017) for more details and full derivation of the idealized model being used here.

The simple model for the advective terms is combined with a linear model for the diabatic terms [Eq. (16)], which has been shown to be a good approximation at the time scale associated with these RD cycles (Inoue and Back 2015, 2017). The slope of the critical GMS line is represented by $\tan(\theta_c)$ in Eq. (16):

$$(\langle Q_R \rangle + S)_M \simeq \tan\theta_c \, \nabla \cdot \langle s\mathbf{v} \rangle. \tag{16}$$

4. Results

a. TOGA COARE results

The characteristics and evolution of different phase angle components through different phases of the RD cycle are plotted in Figs. 5 and 6, and the average 95% confidence interval is specified in the figure captions. Figure 5 shows the bin averaged value of different phase angle components on the y axis as a function of binned values of life cycle phase angle on the x axis. It should be noted that for the purpose of plotting Fig. 5, values on the y axis have been adjusted to be in the range going from $-90°$ to 90°. Values lesser or greater than this range were shifted to be between $-90°$ to 0° and 0° to 90°, respectively. Doing so allows easier interpretation of the y axis in terms of efficiency of MSE import or export. As discussed previously, the 0° angle values represents least efficiency and $\pm 90°$ values represent maximum efficiency. Therefore, displacement from 0° on the y axis in Fig. 5 means that the phase angle component is more efficient at importing MSE for negative values, and more efficient at exporting MSE for positive values.

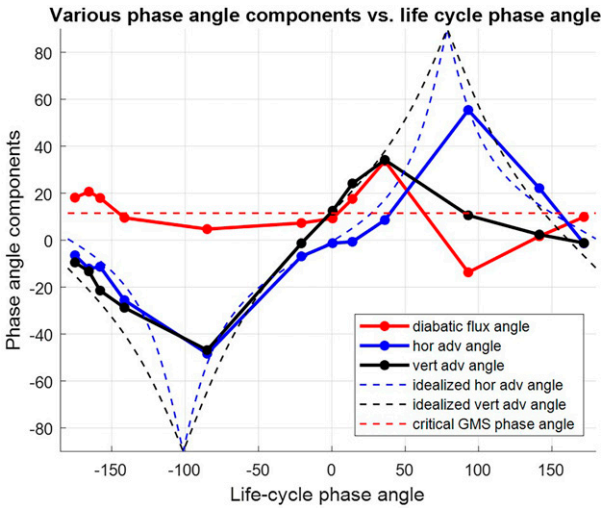

FIG. 5. Various phase angle values as a function of binned life cycle phase angle θ for TOGA COARE data; horizontal phase angle (blue), vertical phase angle (black), diabatic flux angle (red), critical GMS phase angle (red dashed), idealized model horizontal advection phase angle (blue dashed), and idealized model vertical advection phase angle (black dashed). Negative values on x axis correspond to the recharge phase and positive values represent the discharge phase. Average error bars showing the 95% confidence interval for the bin means in vertical phase angle: 19.65; horizontal phase angle: 19.59; and diabatic flux angle: 14.53.

This figure is similar to Fig. 5 from Inoue and Back (2015) having the corresponding phase angle counterparts on the two axes rather than GMS values. Because of the use of phase angles, Fig. 5 present a full composite life cycle and not just the convective half represented in Inoue and Back (2015).

It is observed that the radiative and surface flux terms (solid red curve) stay around a small positive phase value throughout most of the life cycle. This complements the finding of Inoue and Back (2015) that the diabatic terms closely follow the regression line and are well approximated as a linear feedback at these time scales. The positive critical GMS phase angle value (dotted red line) implies that overall the diabatic terms complement the existing MSE anomaly in the column. They add MSE to the column when column MSE anomaly is positive and remove MSE from the column when anomaly is negative. Further, the diabatic fluxes are larger when the existing anomaly is larger.

In comparison, both horizontal and vertical advective phase angles (blue and black curves, respectively) show a cyclic nature, and to some extent are in phase with the life cycle phase angle. The vertical and horizontal phase angles (y axis) have negative values when the life cycle phase angle (x axis) is negative and vice versa. In terms of energy advection, this implies that both horizontal and vertical advection add MSE when the RD cycle is in the recharge phase and remove MSE when the cycle is in the discharge phase. Additionally, the efficiency of the advective terms is also well correlated with that of the overall cycle with the advective terms being less efficient for life cycle phase angle values around 0° and $\pm 180°$.

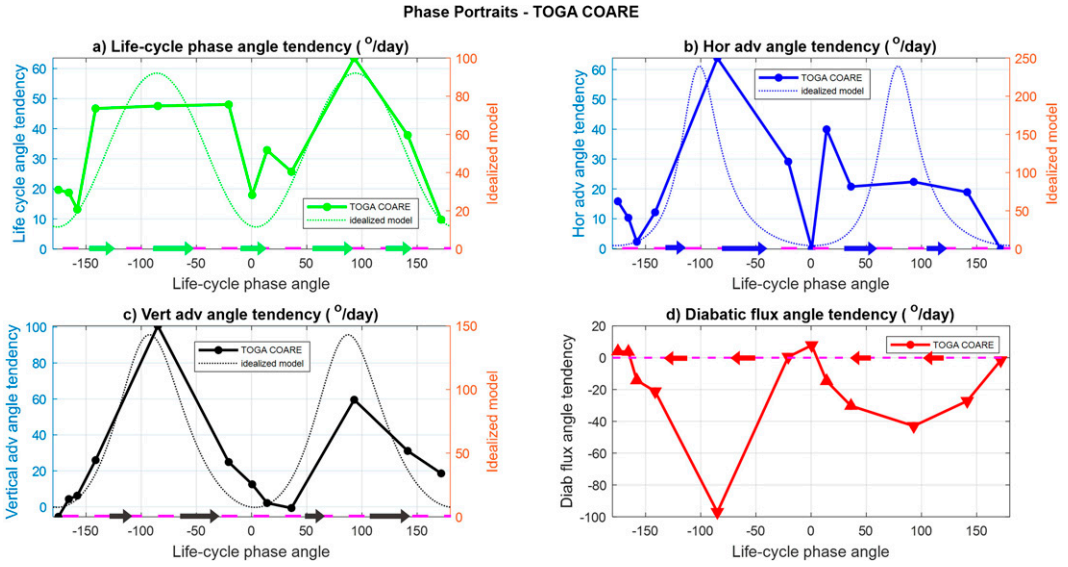

FIG. 6. Phase portraits ($\dot{x}$ vs x) of various phase angles as function of binned life cycle phase angle θ for TOGA COARE data: (a) life cycle phase angle tendency $\delta\theta/\delta t$ (green), (b) horizontal advection phase angle tendency $\delta\theta_H/\delta t$ (blue), (c) vertical advection phase angle tendency $\delta\theta_V/\delta t$ (black), and (d) diabatic flux phase angle tendency $\delta\theta_{\text{diab}}/\delta t$ (red). Corresponding values calculated from the idealized model are plotted for (a)–(c) in dotted lines with magnitudes on the y axis on the right side. Arrows on the x axis represent the impact of the corresponding term on the value of θ on the x axis. Average length of error bars representing the 95% confidence intervals are (a) 69.7, (b) 64.6, (c) 68.7, and (d) 69.6.

The close relationship between the cyclic nature of the RD cycle and the advective terms points toward an important role being played by the advective terms in governing the evolution of the life cycle. This is analyzed more closely by calculating the time derivatives of various phase angles explicitly using a central difference scheme on the phase angle time series. Phase portraits as shown in Fig. 6 are plotted with the computed derivatives. Figure 6 has the same binned values of life cycle phase angle on the x axis as Fig. 5. However, the y axis shows the time tendency of the respective phase angle component, or in other words the contribution to life cycle phase angle tendency from the respective component. Therefore, the positive values on y axis imply an increase in life cycle phase angle value and vice versa. This is also qualitatively shown through the arrows on the x axis in these plots. The arrows point toward the direction in which life cycle phase angle values will tend to evolve under the influence of that particular term.

Taking the time derivative of Eq. (5), the time tendency of life cycle phase angle can be represented as $d\theta/dt = d\theta_{\text{GMS}}/dt$. Therefore, the time tendency of vertical and horizontal advection phase angles contribute directly to the time tendency of the life cycle phase angle as they are a part of θ_{GMS}. The critical GMS phase angle, being a constant, does not contribute to the time evolution. However, that does not mean that the time evolution of the diabatic terms has no effect on the evolution of life cycle phase angle. As discussed later in this section, there is an indirect, or a nonprognostic effect of the diabatic flux phase angle time tendency on the life cycle phase angle through its influence on the critical GMS angle.

Figure 6a shows the time tendency of the life cycle phase angle as a function of binned life cycle phase angle values. It is observed that the life cycle phase angle has a positive time tendency and continues to increase throughout the life cycle. This is consistent with our visualization of the composite life cycle as an elliptical orbit moving in the counterclockwise direction with phase angle going from −180° to 180°. This is an alternate way compared to the vector plots used in Inoue and Back (2017) to visualize the evolution of life cycle on the GMS phase plane. There is also a slow–fast behavior associated with the life cycle evolution that is observed here. The life cycle evolves slowly near phase angle values ±180° and 0° (vertices of the ellipse), shown by the smaller tendency values near these points and faster between them. This slow–fast behavior can be associated with existence of equilibrium points in the system and is discussed in more detail in section 5a. Additionally, Fig. 6a can also be used to get an estimate of the time period for a composite life cycle by integrating the inverse of life cycle angle tendency over a full cycle. Doing so gives the time period of a composite life cycle in TOGA COARE data to be around 11 days.

Figures 6b and 6c show that the contribution to life cycle phase angle tendency by the horizontal and vertical advection phase angles, respectively, is very similar to the angle tendency in Fig. 6a. The slow–fast behavior seen in the life cycle phase angle tendency is also replicated in the phase portrait of the advective terms. Therefore, the advective terms seems to be acting as the drivers of the RD cycle. Although it is difficult to determine which, between vertical and horizontal advection, is the more dominant factor based on this figure alone, neither seems

to be negligible in comparison to the other. More detailed discussion on the role of horizontal advection versus that of vertical advection and their physical interpretation is given in section 5.

Figure 6d shows the negative bin averaged time tendency of the diabatic flux phase angle, which includes the radiative and surface flux terms. A negative tendency is plotted because of the difference in sign of the diabatic terms in Eq. (2). The diabatic flux phase angle tendency does not directly impact the life cycle phase angle as discussed above. However, it does describe the scatter distribution from which the regression slope is being calculated. If the diabatic flux was distributed such that it fits the regression line perfectly then the diabatic flux angle tendency would be zero as diabatic flux evolves along the same line. Therefore, nonzero diabatic flux angle tendencies represent departures from the linear approximation. These nonlinearities impact the calculation of the regression slope and can therefore support changes in the life cycle phase angle value in the direction shown by the arrows in Fig. 6d.

Based on Fig. 6d, it is observed that the diabatic flux angle tendency supports a leftward evolution of the life cycle phase angle over almost the entire RD cycle. Therefore, the second-order effect of the radiative and surface flux feedbacks seems to be to resist the observed direction in which the life cycle evolves and slow it down. This resistance is more like a frictional force that opposes the natural evolution of the system but will not cause the system to move in the opposite direction by itself. Similar results have been found in previous studies (Andersen and Kuang 2012; Kiranmayi and Maloney 2011). The first-order impact of the radiative and surface flux feedbacks is the critical GMS line slope being positive, which represents the diabatic terms acting as a stronger MSE source as convection gets stronger. Long wave cloud convective feedback (lower outgoing radiation for more convection), and wind-induced surface heat exchange feedback (WISHE; higher surface fluxes for more convection) are some dominant mechanisms that can result in this positive slope.

Results from the idealized model for TOGA COARE data (described in section 3d) are represented as dotted lines in Figs. 5 and 6. Since the diabatic terms in the simple model are modeled as a line, the diabatic flux angle tendency is zero and there is no dotted line counterpart for Fig. 6d. The model seems to do quite well in replicating all major features in the two figures. There is a high qualitative agreement between the dotted and solid lines in both the figures. The major differences in shape of the curves can be attributed to the fact that TOGA COARE data have been binned whereas the model time series is not binned. Even quantitatively, the model performs quite well. For Figs. 6a–c the dotted lines are plotted following the y axis on the right-hand side. Although there is a difference in magnitude between the two axes and parts of the cycle in moisture mode appear to be much faster than the observation, the faster parts are compensated by the slower parts such that the overall time scale of the life cycle is same in the model and observations. Therefore, the idealized model has a great success in replicating the RD cycle behavior.

b. *Results from ERA-Interim and satellite-based datasets*

In addition to examining TOGA COARE data, RD cycles are also investigated across different tropical ocean basins using a mix of data products from reanalysis and satellites, as outlined in section 2. The mixed dataset helps test the robustness of these features by studying a longer time series data as well as giving a look at geographic variability. Unlike for TOGA COARE data, the MSE budget in this mixed dataset is not closed because data from different sources is used for different terms. Therefore, precipitable water tendency is used to calculate MSE tendency [left-hand side of Eq. (1)] and the life cycle phase angle instead of Eq. (5). Doing so also allows us to calculate the budget residual and its corresponding phase angle to keep the budget closed. With the 10–90 day filter, using precipitable water tendency to calculate MSE tendency is a reasonable assumption as WTG approximation is valid at these time scales. We use 5% percentile bins for analyzing the mixed dataset. Each bin has more than 4000 samples in all different ocean basins.

Similar to Fig. 5, Fig. 7 shows the characteristics of the different phase angle components as a binned function of life cycle phase angle for the four active ocean basins outlined earlier. The 95% confidence interval for the bin mean value is also represented through the error bars. The diabatic flux angle (red) has a small, positive value throughout most of the life cycle in all ocean basins, similar to TOGA COARE data. This means that the diabatic terms support the existing MSE anomaly in the column during all phases of the life cycle. Horizontal advection (blue) also has a very robust behavior across the different ocean basins and is well correlated with the life cycle phase angle as discussed previously for TOGA COARE data. One of the key differences among the ocean basins and with TOGA COARE data is seen in the vertical advection angle (black).

It is interesting to note that the curve for vertical advection angle looks similar in pairs: one being the Indian Ocean–western Pacific basin, and the other being the eastern Pacific–Atlantic Ocean basin. In the eastern Pacific and Atlantic Ocean basins, the vertical advection angle has a very small slope, and looks more similar to the diabatic terms rather than horizontal advection. In contrast, in the Indian Ocean and western Pacific basins, the vertical advection angle is seen to have a relatively stronger role, particularly for negative life cycle phase angle values on x axis. This difference between the two groups could possibly be related to geographic variability in vertical motion profiles in these regions as observed in previous studies (Back and Bretherton 2006), and is discussed more in the next section. The vertical advection term in all four ocean basins is also very different from TOGA COARE data. This has also been noted in previous studies and could be a result of differences in the scale of the disturbance being observed in the two datasets (Inoue et al. 2021). The Kelvin wave signal could be more dominant in TOGA COARE data, and the MJO or intraseasonal oscillations (ISO) signal could be more dominant in the mixed dataset.

Nevertheless, even though the relationship is not as strong as in TOGA COARE, we can still observe that the negative

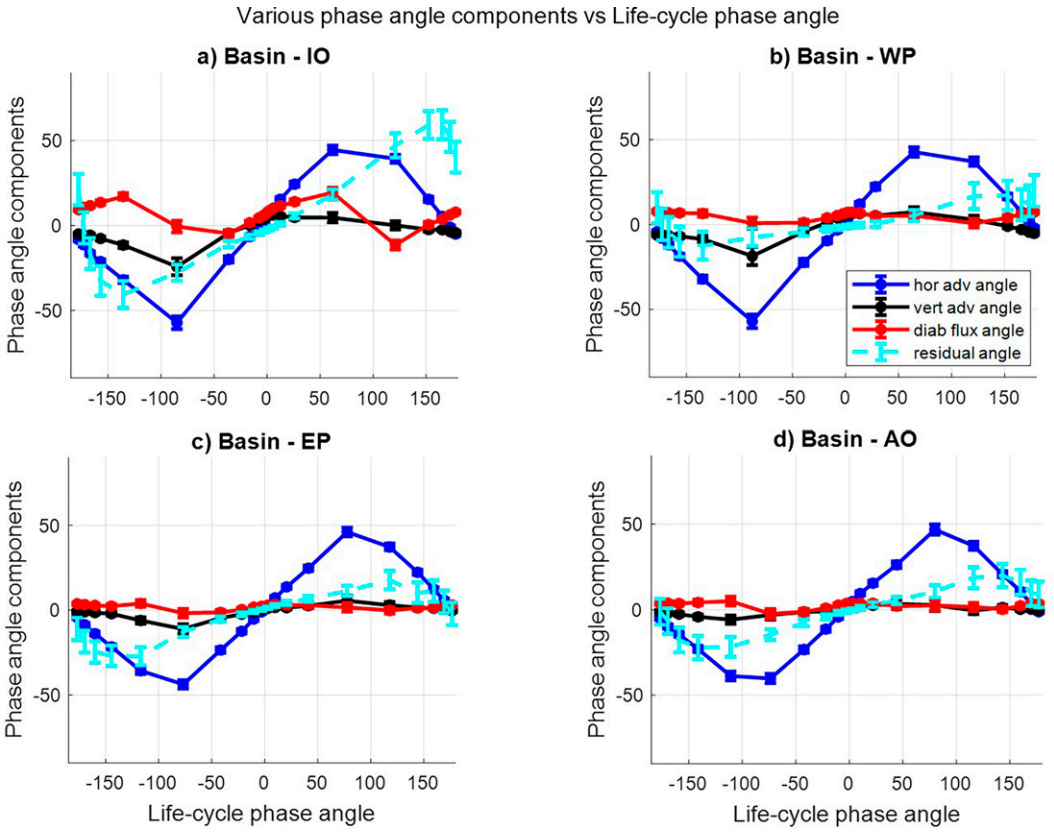

FIG. 7. As in Fig. 5, but with satellite and reanalysis mixed data over different tropical ocean basins: (a) Indian Ocean (IO), (b) western Pacific (WP), (c) eastern Pacific (EP), and (d) Atlantic Ocean (AO). For each subplot, a residual phase angle is also plotted in cyan corresponding to the residual term in the MSE budget from Eq. (1). Error bars represent the 95% confidence interval for each bin mean value.

to positive transition in vertical advection phase angle is weakly in phase with the negative to positive transition of life cycle phase angle on x axis in all four ocean basins. It is observed that the residual term (cyan) also has the systematic relationship with life cycle phase angle like the advective terms. Interestingly, the uncertainties associated with the bin mean residual are also the largest compared to other terms.

Phase portraits of relevant parameters with 95% confidence intervals across different ocean basins are shown in Fig. 8. Qualitatively, the phase portraits for the satellite–reanalysis mixed dataset look similar to those for TOGA COARE. As expected, a positive tendency of the life cycle phase angle (Fig. 8a) is observed in all ocean basins corresponding to counterclockwise life cycle evolution on the phase plane. The same feature is seen for the two advective term tendencies as well in all four ocean basins. Horizontal advection angle tendencies are shown in Fig. 8b and vertical advection tendencies are shown in Fig. 8c. The slow–fast life cycle behavior seen in TOGA COARE data is also observed robustly in all ocean basins. A similar pattern as TOGA COARE is also observed for the diabatic flux angle tendency (Fig. 8d) in all ocean basins representing their resistive effect on RD cycle evolution.

The time evolution of vertical advection phase angle has a significant impact on the life cycle phase angle tendency in Fig. 8 despite the vertical advection phase angle not showing a strong relationship in Fig. 7. Further, the similarities in Figs. 6 and 8 suggest that similar mechanisms might be relevant for both TOGA COARE and mixed dataset in this aspect even though the scale and mode of the disturbance being observed is different between the two. The main difference between the mixed dataset and TOGA COARE phase portraits seems to be in the magnitude of the phase portraits.

The time period of the composite cycle in satellite data is around 40 days (±2 days for all basins), which is much larger compared to 11 days in TOGA COARE. One possible reason for this could simply be on account of the fact that the mixed dataset is a much longer time series compared to TOGA COARE. This would allow longer time scales to be more visible in the mixed dataset compared to TOGA COARE. When the 10–90 day bandpass filter used for mixed data is removed, the phase portraits still qualitatively remain the same but the time period of the cycle changes to around 65 days for all ocean basins (not shown). Conversely, when a fast filter is used (4–20 day bandpass filter) the time period of the cycle reduces to 11–15 days in the four ocean basins with the same qualitative results.

A source of residual in the satellite data could be based on the fact that in this study radiation budgets are calculated

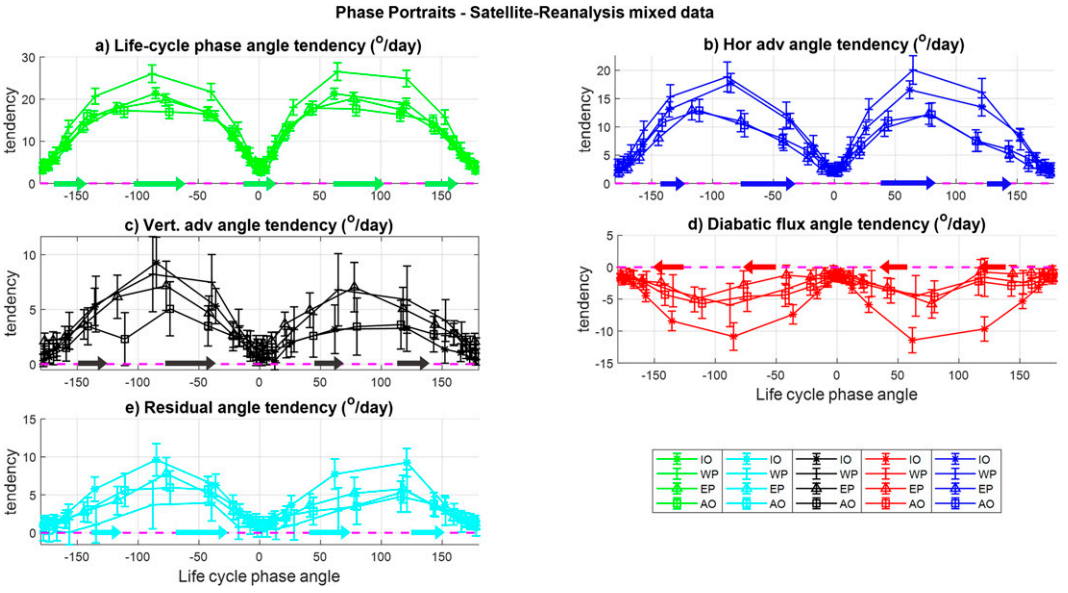

FIG. 8. As in Fig. 6, but with mixed data over different tropical ocean basins: Indian Ocean (IO), western Pacific (WP), eastern Pacific (EP), and Atlantic Ocean (AO). (e) The phase portrait of the residual phase angle for all four ocean basins.

from data at each pixel, and are not spatially averaged over the ocean basin. L'Ecuyer and Stephens (2003) note that there can be considerably higher uncertainties in the radiation budget at individual pixel level compared to the regional mean. Another reason of uncertainty in the satellite data could be related to the fact that satellite observations measure the state at a particular instant in time, and for many regions in the tropics, satellite overhead passes could be too few in number to be able to calculate daily means accurately. In contrast, the advection terms from reanalysis will be based on daily averages leading to a higher residual. Even TOGA COARE data are at a 6 h resolution. This could also lead to some of the observed differences in the mixed data compared to TOGA COARE. The effect of some of these uncertainties could be better understood by only looking at reanalysis data rather than a mix of satellite and reanalysis data.

Figure 9 shows the same plots as Fig. 8 but only with reanalysis data from ERA-Interim. To better constrain the diabatic flux terms in reanalysis, these are calculated as a residual in Eq. (1) since the circulation is better constrained in reanalysis compared to radiative fluxes. With a higher time resolution, daily means from reanalysis data compare better with those from TOGA COARE data than satellite data. Also, with the diabatic terms being calculated as a residual, there can be more certainty at the individual pixel level. The phase portraits in Fig. 9 are very similar to the ones in Fig. 8, both qualitatively and quantitatively. Just like the mixed dataset, results from reanalysis data differ from TOGA COARE results mainly in terms of their magnitude. The time scale of the life cycle in reanalysis data is also around 40 days, similar to the time scale in mixed data.

Although reanalysis data seem to do a good job in representing this cyclic variability here and in previous studies, there can also be multiple areas of concern. Wolding et al. (2022) show that there are considerable differences in the convective cycles in different reanalysis products. In particular, lack of observations in marine atmospheric boundary layer leads to poor constraints on thermodynamic variables in lower troposphere in the reanalysis (Pincus et al. 2017). Wolding et al. (2022) note that this could also contribute to the differences between reanalysis and observations contributing to the residual in Figs. 7 and 8. In that case, the residual will be dependent on reanalysis model parameterization and reanalysis increment, which could help explain the systematic relationship being seen in the residual term.

Despite the data limitations and inaccuracies, the reanalysis data and observations both do show a cyclic behavior. Compositing over life cycle phase angle, overall we observe similar mechanisms contributing to the evolution of the composite cycle in terms of column MSE budget. The invariance of key patterns in different datasets and over different regions suggest that these mechanisms are relevant at different time and spatial scales. Coupling between moisture and convection and the resulting dynamics from that coupling could be a viable place to start in understanding this better.

5. Discussion

a. Recharge–discharge cycles—A dual equilibrium system

The idealized model for the moisture RD cycles is successfully able to replicate the life cycles in TOGA COARE data. The idealized model consists of the interactions between the linearized diabatic term and the advection terms consistent with moisture mode dynamics. On the GMS phase plane, this

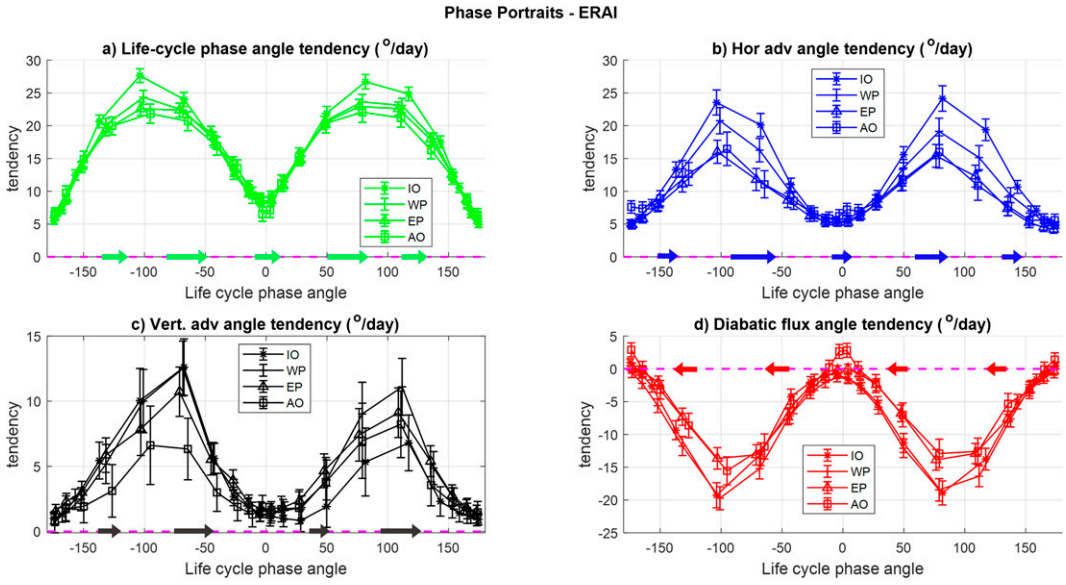

FIG. 9. As in Fig. 8, but with reanalysis data only from ERA-Interim over different tropical ocean basins: Indian Ocean (IO), western Pacific (WP), eastern Pacific (EP), and Atlantic Ocean (AO). The diabatic fluxes are calculated as a residual from the MSE budget so no separate residual phase angle.

is visualized through the line representing the diabatic term, and elliptical orbits for the advective terms in Fig. 1. Points of intersection between the line and the ellipse are points where the diabatic terms and advective terms are equal to each other. The MSE budget [Eq. (1)] is balanced at these points and the time tendency of column MSE, $\partial\langle h\rangle/\partial t$ will be zero. Therefore, these are the equilibrium states for the idealized model. In terms of phase angle values, the points of intersection will be the 0° and 180° life cycle phase angle values. And indeed, we see equilibrium point–like behavior as the system evolves slowly near these phase angle values in data. The life cycle phase angle tendency is smaller and closer to zero in phase portraits around these values in not only TOGA COARE (Fig. 6) but also in mixed (Fig. 8) and reanalysis only datasets (Fig. 9).

Arrows in Figs. 6a, 8a, and 9a also show that both the equilibrium points are half-stable points. The system is attracted toward the equilibrium on the left side and is pushed away from the equilibrium on the right side. Therefore, the equilibrium states do not appear to be fully stable (attracting from all directions) or unstable states (pushing away in all directions).

The equilibrium point at 0° phase angle corresponds to a wet state with enhanced convection, and the equilibrium point at 180° phase angle corresponds to a dry state with suppressed convection. On a simpler level, physically the wet equilibrium state could be expected to exist based on quasi-equilibrium type of ideas and self-organization of convection as discussed in Peters and Neelin (2006) and Wolding et al. (2022). They argue that a slow buildup of convective instability due to large-scale processes and its fast dissipation by convection results in a system that is attracted toward a high critical column water vapor value or a wet equilibrium state. Based on our results, we hypothesize that at intraseasonal time scales the large-scale advective terms modify the self-organizing behavior around the wet state critical point by introducing the dry-state critical point. Because of mass continuity, a convecting atmosphere also controls the amount of subsidence in other areas. At the intraseasonal scales, advection of MSE between the convecting and subsiding regions is able to drive the drying of the convecting region below the critical column water vapor value. Therefore, the critical point no longer behaves as an attractor for all perturbations. Rather there are drying perturbations, which are supported by advective terms, that lead to transition of the system from the wet state critical point to the dry-state critical point. We expect the magnitude of the dry state to be controlled by the magnitude of the wet state. Averaging over such cycles and moving to a larger scale should result in an overall wet state for the tropics consistent with quasi-equilibrium ideas.

b. *Role of horizontal versus vertical advection*

Phase portraits in Figs. 6, 8, and 9 show the contribution of horizontal and vertical advection terms to evolution of the RD cycle across the different datasets. Qualitatively, the two advective terms show a similar behavior, and quantitatively the tendency due to vertical advection is a bit smaller in magnitude but not negligible. This is somewhat in contrast with results of Inoue et al. (2021), who find horizontal advection to be the main driver of convective variability associated with these RD cycles. We explore why this may be below.

Our results suggest that vertical advection has a nonnegligible contribution to the time evolution of life cycle phase angle. Figure 7 shows that the vertical phase angle is small compared to the horizontal phase angle. Further it shows only a very weak correlation with the total phase angle in most of the ocean basins. This matches with the finding in Inoue et al. (2021) that

vertical advection does not do a good job in predicting the state of the system on the GMS phase plane. However, looking explicitly at the evolution of the cycle by computing the time tendency of the life cycle phase angle reveals that vertical advection is playing a nonnegligible role there. In other words, vertical advection may not do a very good job of indicating whether the cycle is currently in the recharge or the discharge phase. However, given the current phase, it has a significant contribution to how it will evolve with time and on shape of the cycle. This is perhaps because of the intrinsic relationship between vertical motion profile shape and efficiency of MSE transport through vertical advection in the column. GMS-based phase angles then, as a metric, are much better adapted at focusing on this aspect of the recharge–discharge cycle behavior and the inherent properties of convection including vertical advection.

c. *Ubiquitous nature of horizontal advection*

Convective behavior associated with the RD cycles is observed ubiquitously throughout the tropics, both in this work, as well as previous studies (Inoue and Back 2017; Wolding et al. 2020; Inoue et al. 2021). Perhaps more surprising is the ubiquitous nature of horizontal advection (Inoue et al. 2021). Due to geographic variations in moisture gradients and the circulation, it is not necessary to expect horizontal advection to have similar patterns or similar time scales in different ocean basins. The ubiquitous nature then suggests that horizontal advection during these recharge–discharge cycles is dominated by the part of the circulation that is intrinsically linked to the local convective features, and can thus be expected to be uniform across the different ocean basins. In that case, convection could be playing a dominant role in governing the large-scale environment at these scales rather than the other way around.

A possible way to test this could be by decomposing the horizontal advection into being associated with a local and nonlocal flow (appendix A of Wang et al. 2016). Local flow is the part of horizontal circulation, which can be attributed to divergence and vorticity of the circulation associated with local convection within the box. In contrast, the nonlocal flow is the part of circulation, which is attributed to divergence and vorticity caused by convection elsewhere. Horizontal advection then represents how these transport MSE in the presence of moisture gradients or anomalies (temperature gradients are small in the tropics following WTG approximation).

We hypothesize that horizontal advection during these RD cycles is dominated more by the local flow part, and intrinsically linked to local convection. Horizontal advection due to this local flow will include advection of MSE by the divergent part of local flow [also termed as lateral entrainment in Raymond and Zeng (2005)], and advection of MSE by the rotational part of the local flow. In such a scenario, the nonlocal horizontal advection just pushes around moisture anomalies. When the amount of vertical motion is low, the nonlocal horizontal advection can push the cycle in the recharge or discharge phase (similar to findings of Inoue et al. 2021). However, once the local vertical motion is nonnegligible, further evolution of convection, and hence moisture, is dominated by the vertical advection and the local horizontal advection. Future work computing this local and nonlocal horizontal advection explicitly during recharge–discharge cycles, similar to Wang et al. (2016), can help test these ideas further.

d. *Role of vertical motion profile shape variability and vertical tilt*

We expect the recharge phase to have bottom-heavy vertical profiles leading to negative GMS values and import MSE into the column. Oppositely, the discharge phase should have top-heavy vertical motion profiles leading to positive GMS values and export of column MSE (Inoue and Back 2015). Anomalous vertical motion profiles during TOGA COARE averaged over binned life cycle phase angle values are shown in Fig. 10. Life cycle phase angle values greater than 90° and less than −90°, which correspond to the convectively inactive part of the cycle, primarily show subsidence. During the convectively active part of the cycle, vertical motion profiles are more bottom-heavy during negative life cycle phase angles (recharge phase), and transition to a more top-heavy profile during positive life cycle phase angle (discharge phase) as expected. Transition of vertical motion profiles from bottom-heavy to top-heavy, also referred to as "vertical tilt," has also been observed to be important in other types of tropical convective organization. Inoue et al. (2020) find that the fast moving convectively coupled wave modes like the Kelvin waves, inertial gravity waves, and the mixed Rossby–gravity waves all show more significant vertical tilt compared to the slower moisture modes like MJO.

This vertical tilt is very important for the half-stable nature of the equilibrium state discussed earlier. After reaching the peak moisture anomaly at the wet equilibrium state, if vertical motion profile continues to be bottom-heavy then any drying perturbation will eventually die out rather than grow to push the system toward the dry equilibrium state. Therefore, vertical motion profile shape variability is key for driving the cyclic behavior seen in these RD cycles.

Varying vertical motion profile shape implies a vertical GMS value that is time dependent. In the idealized model, time-dependent GMS is associated with a nonzero $\Gamma_{\mathrm{eff},i}$ and $\Gamma_{v,i}$ in Eq. (12). $\Gamma_{\mathrm{eff},i}$ in turn is associated with the propagation of the wave mode in the idealized model. Therefore, vertical tilt can also be important for propagation of faster moisture dominated modes like the convective cycles in TOGA COARE.

6. Conclusions

This study aims to develop a better understanding of the role of vertical advection, horizontal advection, and diabatic fluxes in the evolution of moisture recharge–discharge cycles and compares these in the TOGA COARE data, satellite data, and reanalysis data. To do so, we define and study various phase angle parameters on the GMS phase plane. The phase angle parameters are analogous to GMS, and represent efficiency of MSE transport by a particular term in MSE budget. They have the advantage that the phase angle value does not go to infinity even if the denominator in GMS becomes

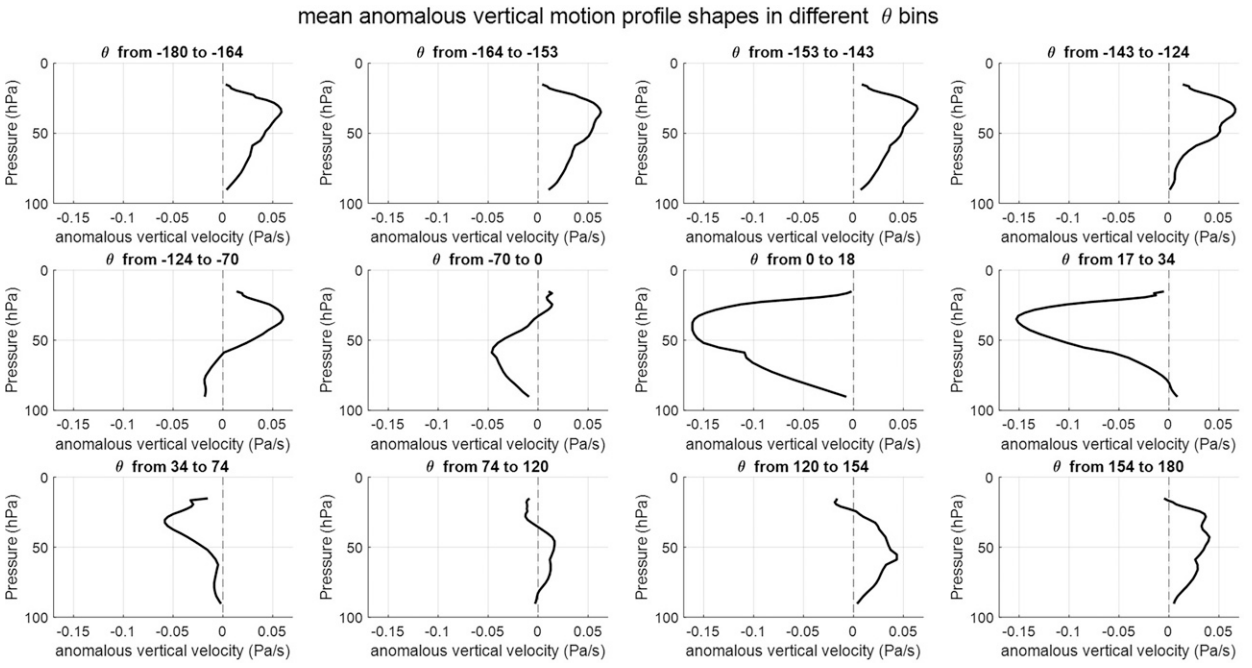

FIG. 10. Vertical profiles of mean vertical velocity (Pa s^{-1}) composited over life cycle phase angle θ bins from the x axis in Figs. 5 and 6. Positive vertical velocities indicate descent and negative values indicate ascent. θ between $-90°$ and 90° is the convectively active phase, and θ greater than 90° and less than $-90°$ is the convectively inactive phase.

very small. Therefore, the phase angle is particularly effective in studying the recharge–discharge cycles, which are also associated with a cycle of changing GMS values.

The results show the following basic characteristics associated with moisture recharge–discharge cycles.

- Diabatic fluxes, which include column radiation and surface fluxes, support the existing MSE anomalies throughout different phases of the cycle.
- When vertical and horizontal advection are acting as a source of MSE, the cycle is in the recharge phase with moisture and precipitation increasing with time. In contrast, when vertical and horizontal advection are acting as a MSE sink, the cycle is in the discharge phase with moisture and precipitation decreasing with time.
- The cycle exhibits a slow–fast behavior. The system evolves slowly near two equilibrium points and faster between them. One of the two equilibrium states correspond to an anomalously moist state with enhanced convection, and the other equilibrium state corresponds to an anomalously dry state with suppressed convection. Near both the equilibrium states, the advective and diabatic flux terms in the MSE budget cancel each other resulting in a small MSE tendency, and slow evolution of the system.
- Both vertical and horizontal advection terms are observed to act like drivers of the RD cycle. Although the impact of the vertical advection term is a bit smaller compared to horizontal advection, it is not negligible. Consistent with previous studies, we find that vertical advection is not a robust indicator of whether the cycle is in the recharge or the discharge phase. However, time evolution of vertical advection does play a significant role (along with evolution of horizontal advection) in driving the evolution of the overall cycle.
- The tendency of diabatic fluxes has an indirect effect on the evolution of the cycle. It is found to resist the observed evolution of the overall recharge–discharge cycle and slow it down. The diabatic fluxes themselves amplify the existing MSE anomaly in the system, but the sensitivity of convection to diabatic fluxes slows down the convective evolution during the recharge–discharge cycles, consistent with previous studies.

These features are mostly consistent across the various datasets used in this study, ranging from the shorter-time-scale TOGA COARE data to the longer time series data from satellites and reanalysis covering different tropical ocean basins. The consistency of the results across different datasets, and the different ocean basins suggests that similar mechanisms are important for understanding the RD cycles over different regions and at different scales. The evidence showing the limitations in our current models in getting this type of variability correctly (Wolding et al. 2020) calls for further research in this area. A starting point could be looking deeper into evolution of moisture and moisture dynamics. The data satisfy many of the key criteria to be classified as a moisture mode. Further, an idealized model based on the same key assumptions as moisture modes is found to replicate the features of the RD cycles in TOGA COARE data accurately. This indicates the importance of moisture and moisture mode–like mechanisms in understanding RD cycles and general evolution of convection throughout the tropics despite the differences in scales and dominant wave modes.

Acknowledgments. This research is supported by NSF Grants 1549512 and 1759793. We thank Tristan L'Ecuyer and William Olson for the radiative heating data, and Minghua Zhang for the TOGA COARE data. We would also like to thank Kuniaki Inoue, Brandon Wolding, and three anonymous reviewers whose comments have helped improved the manuscript greatly.

Data availability statement. SSM/I and SSMIS data are produced by Remote Sensing Systems (www.remss.com/missions/ssmi); AMSR data are produced by Remote Sensing Systems and were sponsored by the NASA AMSR-E Science Team and the NASA Earth Science MEaSUREs Program (www.remss.com); TMI data were produced by Remote Sensing Systems and sponsored by the NASA Earth Sciences Program (www.remss.com/missions/tmi); and ERA-Interim data are produced by ECMWF (https://www.ecmwf.int/en/forecasts/dataset/ecmwf-reanalysis-interim).

REFERENCES

Adames, Á. F., and D. Kim, 2016: The MJO as a dispersive, convectively coupled moisture wave: Theory and observations. *J. Atmos. Sci.*, **73**, 913–941, https://doi.org/10.1175/JAS-D-15-0170.1.

——, and E. D. Maloney, 2021: Moisture mode theory's contribution to advances in our understanding of the Madden-Julian oscillation and other tropical disturbances. *Curr. Climate Change Rep.*, **7**, 72–85, https://doi.org/10.1007/s40641-021-00172-4.

Ahn, M.-S., D. Kim, K. R. Sperber, I.-S. Kang, E. Maloney, D. Waliser, and H. Hendon, 2017: MJO simulation in CMIP5 climate models: MJO skill metrics and process-oriented diagnosis. *Climate Dyn.*, **49**, 4023–4045, https://doi.org/10.1007/s00382-017-3558-4.

Andersen, J. A., and Z. Kuang, 2012: Moist static energy budget of MJO-like disturbances in the atmosphere of a zonally symmetric aquaplanet. *J. Climate*, **25**, 2782–2804, https://doi.org/10.1175/JCLI-D-11-00168.1.

Back, L. E., and C. S. Bretherton, 2006: Geographic variability in the export of moist static energy and vertical motion profiles in the tropical Pacific. *Geophys. Res. Lett.*, **33**, L17810, https://doi.org/10.1029/2006GL026672.

Beucler, T., and T. W. Cronin, 2016: Moisture-radiative cooling instability. *J. Adv. Model. Earth Syst.*, **8**, 1620–1640, https://doi.org/10.1002/2016MS000763.

Bretherton, C. S., and A. H. Sobel, 2002: A simple model of a convectively coupled Walker circulation using the weak temperature gradient approximation. *J. Climate*, **15**, 2907–2920, https://doi.org/10.1175/1520-0442(2002)015<2907:ASMOAC>2.0.CO;2.

——, M. E. Peters, and L. E. Back, 2004: Relationships between water vapor path and precipitation over the tropical oceans. *J. Climate*, **17**, 1517–1528, https://doi.org/10.1175/1520-0442(2004)017<1517:RBWVPA>2.0.CO;2.

——, P. N. Blossey, and M. Khairoutdinov, 2005: An energy-balance analysis of deep convective self-aggregation above uniform SST. *J. Atmos. Sci.*, **62**, 4273–4292, https://doi.org/10.1175/JAS3614.1.

Chikira, M., 2014: Eastward-propagating intraseasonal oscillation represented by Chikira–Sugiyama cumulus parameterization. Part II: Understanding moisture variation under weak temperature gradient balance. *J. Atmos. Sci.*, **71**, 615–639, https://doi.org/10.1175/JAS-D-13-038.1.

Curry, J. A., and Coauthors, 2004: SeaFlux. *Bull. Amer. Meteor. Soc.*, **85**, 409–424, https://doi.org/10.1175/BAMS-85-3-409.

Dee, D. P., and Coauthors, 2011: The ERA-Interim reanalysis: Configuration and performance of the data assimilation system. *Quart. J. Roy. Meteor. Soc.*, **137**, 553–597, https://doi.org/10.1002/qj.828.

Fuchs, Ž., and D. J. Raymond, 2017: A simple model of intraseasonal oscillations. *J. Adv. Model. Earth Syst.*, **9**, 1195–1211, https://doi.org/10.1002/2017MS000963.

Hannah, W. M., and E. D. Maloney, 2014: The moist static energy budget in NCAR CAM5 hindcasts during DYNAMO. *J. Adv. Model. Earth Syst.*, **6**, 420–440, https://doi.org/10.1002/2013MS000272.

——, B. E. Mapes, and G. S. Elsaesser, 2016: A Lagrangian view of moisture dynamics during DYNAMO. *J. Atmos. Sci.*, **73**, 1967–1985, https://doi.org/10.1175/JAS-D-15-0243.1.

Hung, M.-P., J.-L. Lin, W. Wang, D. Kim, T. Shinoda, and S. J. Weaver, 2013: MJO and convectively coupled equatorial waves simulated by CMIP5 climate models. *J. Climate*, **26**, 6185–6214, https://doi.org/10.1175/JCLI-D-12-00541.1.

Inoue, K., and L. E. Back, 2015: Gross moist stability assessment during TOGA COARE: Various interpretations of gross moist stability. *J. Atmos. Sci.*, **72**, 4148–4166, https://doi.org/10.1175/JAS-D-15-0092.1.

——, and ——, 2017: Gross moist stability analysis: Assessment of satellite-based products in the GMS plane. *J. Atmos. Sci.*, **74**, 1819–1837, https://doi.org/10.1175/JAS-D-16-0218.1.

——, Á. F. Adames, and K. Yasunaga, 2020: Vertical velocity profiles in convectively coupled equatorial waves and MJO: New diagnoses of vertical velocity profiles in the wavenumber–frequency domain. *J. Atmos. Sci.*, **77**, 2139–2162, https://doi.org/10.1175/JAS-D-19-0209.1.

——, M. Biasutti, and A. M. Fridlind, 2021: Evidence that horizontal moisture advection regulates the ubiquitous amplification of rainfall variability over tropical oceans. *J. Atmos. Sci.*, **78**, 529–547, https://doi.org/10.1175/JAS-D-20-0201.1.

Jiang, X., and Coauthors, 2015: Vertical structure and physical processes of the Madden-Julian oscillation: Exploring key model physics in climate simulations. *J. Geophys. Res. Atmos.*, **120**, 4718–4748, https://doi.org/10.1002/2014JD022375.

Juračić, A., and D. J. Raymond, 2016: The effects of moist entropy and moisture budgets on tropical cyclone development. *J. Geophys. Res. Atmos.*, **121**, 9458–9473, https://doi.org/10.1002/2016JD025065.

Kiladis, G. N., M. C. Wheeler, P. T. Haertel, K. H. Straub, and P. E. Roundy, 2009: Convectively coupled equatorial waves. *Rev. Geophys.*, **47**, RG2003, https://doi.org/10.1029/2008RG000266.

Kim, D., and Coauthors, 2014: Process-oriented MJO simulation diagnostic: Moisture sensitivity of simulated convection. *J. Climate*, **27**, 5379–5395, https://doi.org/10.1175/JCLI-D-13-00497.1.

Kiranmayi, L., and E. D. Maloney, 2011: Intraseasonal moist static energy budget in re-analysis data. *J. Geophys. Res.*, **116**, D21117, https://doi.org/10.1029/2011JD016031.

L'Ecuyer, T. S., and G. L. Stephens, 2003: The tropical oceanic energy budget from the TRMM perspective. Part I: Algorithm and uncertainties. *J. Climate*, **16**, 1967–1985, https://doi.org/10.1175/1520-0442(2003)016<1967:TTOEBF>2.0.CO;2.

——, and ——, 2007: The tropical atmospheric energy budget from the TRMM perspective. Part II: Evaluating GCM representations of the sensitivity of regional energy and water

cycles to the 1998–99 ENSO cycle. *J. Climate*, **20**, 4548–4571, https://doi.org/10.1175/JCLI4207.1.

Maloney, E. D., 2009: The moist static energy budget of a composite tropical intraseasonal oscillation in a climate model. *J. Climate*, **22**, 711–729, https://doi.org/10.1175/2008JCLI2542.1.

Mapes, B., S. Tulich, J. Lin, and P. Zuidema, 2006: The mesoscale convection life cycle: Building block or prototype for large-scale tropical waves? *Dyn. Atmos. Oceans*, **42**, 3–29, https://doi.org/10.1016/j.dynatmoce.2006.03.003.

Masunaga, H., and T. S. L'Ecuyer, 2014: A mechanism of tropical convection inferred from observed variability in the moist static energy budget. *J. Atmos. Sci.*, **71**, 3747–3766, https://doi.org/10.1175/JAS-D-14-0015.1.

Matsuno, T., 1966: Quasi-geostrophic motions in the equatorial area. *J. Meteor. Soc. Japan*, **44**, 25–43, https://doi.org/10.2151/jmsj1965.44.1_25.

Mayta, V. C., Á. F. Adames, and F. Ahmed, 2022: Westward-propagating moisture mode over the tropical Western Hemisphere. *Geophys. Res. Lett.*, **49**, e2022GL097799, https://doi.org/10.1029/2022GL097799.

Neelin, J. D., and I. M. Held, 1987: Modeling tropical convergence based on the moist static energy budget. *Mon. Wea. Rev.*, **115**, 3–12, https://doi.org/10.1175/1520-0493(1987)115<0003:MTCBOT>2.0.CO;2.

Peters, O., and J. D. Neelin, 2006: Critical phenomena in atmospheric precipitation. *Nat. Phys.*, **2**, 393–396, https://doi.org/10.1038/nphys314.

Pincus, R., A. Beljaars, S. A. Buehler, G. Kirchengast, F. Ladstaedter, and J. S. Whitaker, 2017: The representation of tropospheric water vapor over low-latitude oceans in (re-)analysis: Errors, impacts, and the ability to exploit current and prospective observations. *Surv. Geophys.*, **38**, 1399–1423, https://doi.org/10.1007/s10712-017-9437-z.

Raymond, D. J., and X. Zeng, 2005: Modelling tropical atmospheric convection in the context of the weak temperature gradient approximation. *Quart. J. Roy. Meteor. Soc.*, **131**, 1301–1320, https://doi.org/10.1256/qj.03.97.

——, and Ž. Fuchs, 2007: Convectively coupled gravity and moisture modes in a simple atmospheric model. *Tellus*, **59A**, 627–640, https://doi.org/10.1111/j.1600-0870.2007.00268.x.

——, and ——, 2009: Moisture modes and the Madden–Julian oscillation. *J. Climate*, **22**, 3031–3046, https://doi.org/10.1175/2008JCLI2739.1.

——, S. L. Sessions, A. H. Sobel, and Ž. Fuchs, 2009: The mechanics of gross moist stability. *J. Adv. Model. Earth Syst.*, **1** (9), https://doi.org/10.3894/JAMES.2009.1.9.

Sobel, A. H., and C. S. Bretherton, 2000: Modeling tropical precipitation in a single column. *J. Climate*, **13**, 4378–4392, https://doi.org/10.1175/1520-0442(2000)013<4378:MTPIAS>2.0.CO;2.

——, and E. Maloney, 2013: Moisture modes and the eastward propagation of the MJO. *J. Atmos. Sci.*, **70**, 187–192, https://doi.org/10.1175/JAS-D-12-0189.1.

——, J. Nilsson, and L. M. Polvani, 2001: The weak temperature gradient approximation and balanced tropical moisture waves. *J. Atmos. Sci.*, **58**, 3650–3665, https://doi.org/10.1175/1520-0469(2001)058<3650:TWTGAA>2.0.CO;2.

Stevens, B., and S. Bony, 2013: What are climate models missing? *Science*, **340**, 1053–1054, https://doi.org/10.1126/science.1237554.

Su, H., and J. D. Neelin, 2002: Teleconnection mechanisms for tropical Pacific descent anomalies during El Niño. *J. Atmos. Sci.*, **59**, 2694–2712, https://doi.org/10.1175/1520-0469(2002)059<2694:TMFTPD>2.0.CO;2.

Wang, S., A. H. Sobel, and J. Nie, 2016: Modeling the MJO in a cloud-resolving model with parameterized large-scale dynamics: Vertical structure, radiation, and horizontal advection of dry air. *J. Adv. Model. Earth Syst.*, **8**, 121–139, https://doi.org/10.1002/2015MS000529.

Webster, P. J., and R. Lukas, 1992: TOGA COARE: The Coupled Ocean–Atmosphere Response Experiment. *Bull. Amer. Meteor. Soc.*, **73**, 1377–1416, https://doi.org/10.1175/1520-0477(1992)073<1377:TCTCOR>2.0.CO;2.

Wentz, F., K. Hilburn, and D. Smith, 2012: Remote Sensing Systems DMSP SSM/I daily environmental suite on 0.25 deg grid, version 7. Remote Sensing Systems, accessed 4 October 2021, www.remss.com/missions/ssmi.

——, T. Meissner, C. Gentemann, and M. Brewer, 2014: Remote Sensing Systems Aqua AMSR-E daily environmental suite on 0.25 deg grid, version 7.0. Remote Sensing Systems, accessed 4 October 2021, www.remss.com/missions/amsr.

——, C. Gentemann, and K. Hilburn, 2015: Remote Sensing Systems TRMM TMI daily environmental suite on 0.25 deg grid, version 7.1. Remote Sensing Systems, accessed 4 October 2021, www.remss.com/missions/tmi.

Wing, A. A., and K. A. Emanuel, 2014: Physical mechanisms controlling self-aggregation of convection in idealized numerical modeling simulations. *J. Adv. Model. Earth Syst.*, **6**, 59–74, https://doi.org/10.1002/2013MS000269.

Wolding, B. O., E. D. Maloney, and M. Branson, 2016: Vertically resolved weak temperature gradient analysis of the Madden-Julian oscillation in SP-CESM. *J. Adv. Model. Earth Syst.*, **8**, 1586–1619, https://doi.org/10.1002/2016MS000724.

——, J. Dias, G. Kiladis, F. Ahmed, S. W. Powell, E. Maloney, and M. Branson, 2020: Interactions between moisture and tropical convection. Part I: The coevolution of moisture and convection. *J. Atmos. Sci.*, **77**, 1783–1799, https://doi.org/10.1175/JAS-D-19-0225.1.

——, S. W. Powell, F. Ahmed, J. Dias, M. Gehne, G. Kiladis, and J. D. Neelin, 2022: Tropical thermodynamic–convection coupling in observations and reanalyses. *J. Atmos. Sci.*, **79**, 1781–1803, https://doi.org/10.1175/JAS-D-21-0256.1.

Yano, J.-I., and M. Bonazzola, 2009: Scale analysis for large-scale tropical atmospheric dynamics. *J. Atmos. Sci.*, **66**, 159–172, https://doi.org/10.1175/2008JAS2687.1.

Yasunaga, K., S. Yokoi, K. Inoue, and B. E. Mapes, 2019: Space–time spectral analysis of the moist static energy budget equation. *J. Climate*, **32**, 501–529, https://doi.org/10.1175/JCLI-D-18-0334.1.

Zhang, M. H., and J. L. Lin, 1997: Constrained variational analysis of sounding data based on column-integrated budgets of mass, heat, moisture, and momentum: Approach and application to ARM measurements. *J. Atmos. Sci.*, **54**, 1503–1524, https://doi.org/10.1175/1520-0469(1997)054<1503:CVAOSD>2.0.CO;2.